

Available online at www.sciencedirect.com

SciVerse ScienceDirect

www.elsevier.com/locate/matchar

Effect of carbon content on solidification behaviors and morphological characteristics of the constituent phases in Cr-Fe-C alloys

Chi-Ming Lin^a, Hsuan-Han Lai^a, Jui-Chao Kuo^b, Weite Wu^{a,*}

^aDepartment of Materials Science and Engineering, National Chung Hsing University, 250 Kuo Kuang Road, Taichung 402, Taiwan

^bDepartment of Materials Science and Engineering, National Cheng Kung University, Taiwan

ARTICLE DATA

Article history:

Received 15 June 2011

Received in revised form

17 September 2011

Accepted 20 September 2011

Keywords:

Cr-Fe-C alloys

Transmission electron microscopy

Crystal growth

Solidification behavior

Electron backscatter diffraction

ABSTRACT

A combination of transmission electron microscopy, electron backscatter diffraction and wavelength dispersive spectrum has been used to identify crystal structure, grain boundary characteristic and chemical composition of the constituent phases in Cr-Fe-C alloys with three different carbon concentrations. Depending on the three different carbon concentrations, the solidification structures are found to consist of primary α -phase and $[\alpha + (\text{Cr,Fe})_{23}\text{C}_6]$ eutectic in Cr-18.4Fe-2.3 C alloy; primary $(\text{Cr,Fe})_{23}\text{C}_6$ and $[\alpha + (\text{Cr,Fe})_{23}\text{C}_6]$ eutectic in Cr-24.5Fe-3.8 C alloy and primary $(\text{Cr,Fe})_7\text{C}_3$ and $[\alpha + (\text{Cr,Fe})_7\text{C}_3]$ eutectic in Cr-21.1Fe-5.9 C alloy, respectively. The grain boundary analysis is useful to understand growth mechanism of the primary phase. The morphologies of primary $(\text{Cr,Fe})_{23}\text{C}_6$ and $(\text{Cr,Fe})_7\text{C}_3$ carbides are faceted structures with polygonal shapes, different from primary α -phase with dendritic shape. The primary $(\text{Cr,Fe})_{23}\text{C}_6$ and $(\text{Cr,Fe})_7\text{C}_3$ carbides with strong texture exist a single crystal structure and contain a slight low angle boundary, resulting in the polygonal growth mechanism. Nevertheless, the primary α -phase with relative random orientation exhibits a polycrystalline structure and comprises a massive high-angle boundary, caused by the dendritic growth mechanism.

© 2011 Elsevier Inc. All rights reserved.

1. Introduction

Cr-Fe-C alloy is well known for its excellent resistance to abrasion, oxidation and corrosion and has been extensively used in aggressive conditions, such as mining and mineral process, cement production and pulp and paper manufacture industries. Many previous investigations have focused on the microstructural characteristics, mechanical properties and abrasive wear behaviors of Cr-Fe-C alloys [1–8]. Previous research has shown that Cr-Fe-C alloys consist of hypoeutectic, near-eutectic and hypereutectic structures with Cr-Fe solid solution phase, M_{23}C_6 and M_7C_3 carbides [2]. Moreover, the best performances for Cr-Fe-C alloys are achieved, when

there are large quantities of primary M_7C_3 carbides uniformly distributed in the $[\alpha + \text{M}_7\text{C}_3]$ eutectic colonies [2,8].

The morphologies of constituent phases can exhibit a wide variety of geometrical arrangements. Many recent investigations report solidification behaviors and morphological transitions of the constituent phases in Fe-based, Cu-based and other alloys [9–18]. Nevertheless, few studies have concentrated on solidification behaviors and morphological transitions of the constituent phases in Cr-Fe-C alloys. The morphological transitions of constituent phases directly depend on roughness parameters of the solid/liquid interface, entropies of fusion, chemical compositions and volume fractions of the constituent phases [19–21]. Entropy of melting is a

* Corresponding author. Tel.: +886 4 22840500x604; fax: +886 4 22857017.
E-mail address: wuu@dragon.nchu.edu.tw (W. Wu).

Table 1 – Alloy filler components.

| Filler | Powder (%) | | Alloy elements (wt.%) | |
|--------|------------|-----------|-----------------------|---|
| | Cr | CrC (4:1) | Cr | C |
| A | 85 | 15 | 97 | 3 |
| B | 75 | 25 | 95 | 5 |
| C | 65 | 35 | 93 | 7 |

convenient criterion for predicting crystallization behavior of the constituent phases. Values of α ($\alpha = \Delta S_f / R$, ΔS_f , entropy of fusion; R, gas constant), which are less than 2, imply a tendency toward non-faceted crystal growth, while higher α -values favor production of faceted crystal growth-forms.

Electron backscatter diffraction has been commonly used to characterize crystallographic orientation, texture and grain boundary misorientation of the multi-phase compounds in several different materials [22–27]. The characteristic of Grain boundary examined by electron backscatter diffraction is useful to understand growth mechanism of the constituent phase. But few previous electron backscatter diffraction investigations have devoted to the grain boundary analysis to estimate growth mechanism of the constituent phase. Therefore, the aims of the current work are to investigate solidification behaviors and morphological characteristics of the constituent phases in Cr-Fe-C alloys containing various carbon contents. Solidification behaviors and morphological transitions of the constituent phases are systematically characterized by optical microscopy, field-emission scanning electron microscopy, transmission electron microscopy, electron backscatter diffraction, wavelength dispersive spectrum and differential scanning calorimeter.

2. Experimental Procedures

Cr-Fe-C alloys were prepared by gas tungsten arc welding technique to deposit various pure Cr and CrC (Cr:C=4:1) alloy fillers onto the S45C medium-carbon steel. The dimension of S45C medium-carbon steel was 105 mm × 85 mm × 19 mm. Distinct pure Cr and CrC (Cr:C=4:1) alloy fillers were mixed in a mechanical mixer to obtain a uniformly mixed powder. Then, these alloy fillers were subjected to a high pressure of 105.39 kg cm⁻² to form the compact alloy fillers with the

dimensions of 30 mm × 25 mm × 3 mm. Table 1 lists the alloy filler components. Bead-on-plate with oscillation gas tungsten arc welding was utilized to deposit the claddings. Fig. 1 shows the schematic illustration of gas tungsten arc welding for hard-facing. Table 2 reveals the welding parameter in this study.

Specimens for metallographic examination by optical microscopy and field-emission scanning electron microscopy were ground on silicon carbide papers to 1500 grit and then progressively polished with 1 and 0.3 μm Al₂O₃ powder. The etching agents were 20 g ammonium hydrogen fluoride, 0.5 g potassium pyrosulfite and 100 ml H₂O at 80 °C. Thin foils for transmission electron microscopy observation were prepared by twin-jet electro-polishing using a solution of 5% perchloric acid, 25% glycerol and 70% ethanol at room temperature and 28 V etching potential. For the electron backscatter diffraction sample preparation, the surfaces of materials were mechanically polished through a standard metallographic procedure, to achieve a final level of 0.02 μm. Electron backscatter diffraction measurement was performed on the top surface of hard-facing alloy in a field emission scanning electron microscopy of JEOL 7001 F with an EDAX/TSL Technology electron backscatter diffraction system operated at 20 kV. The measured area for electron backscatter diffraction analysis was 40 μm × 40 μm with a step size of 50 nm. The OIM™ software was used to analyze the image quality, phase map, inverse pole figure orientation map and grain boundary misorientation angle map.

Chemical compositions of the cladding layers and constituent phases were analyzed by wavelength dispersive spectrum. The phase transitions during solidification process in Cr-Fe-C alloys with three distinct carbon contents were determined by differential scanning calorimeter under an argon atmosphere. The flow rate of argon was 4 L/min and both heating and cooling rates were 10 °C/min. The highest temperature was 1600 °C.

3. Results and Discussion

3.1. Chemical Composition and Microstructure Observation

Table 3 lists chemical compositions of the as-clad Cr-Fe-C alloys. Results show that the carbon content varies from 2.3 to 5.9 wt%. For the hypoeutectic structure of alloy A, the carbon

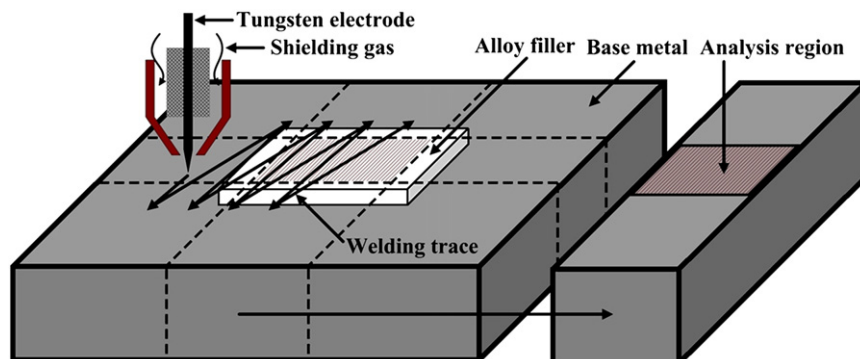


Fig. 1 – Schematic illustration of the gas tungsten arc welding for hard-facing.

Table 2 – Experimental parameters of the gas tungsten arc welding.

| Parameter | Value |
|---|------------|
| Electrode | |
| Type | W-2%ThO |
| Diameter | 3.2 mm |
| Angle | 30° |
| Voltage | 15 V |
| Current | 220 A |
| Heat input | 4.6 MJ/m |
| Protective gas | |
| Type | Ar |
| Flow | 15 L/min |
| Welding speed | |
| Travel speed | 30 mm/min |
| Oscillating speed | 230 mm/min |
| Heat input $Q = \eta \times I \times V / S$, η : welding efficiency (0.7), I: current, V: voltage, S: travel speed. | |

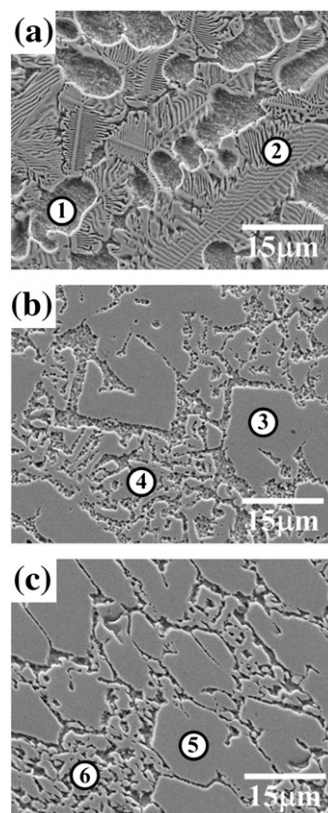
content is about 2.3 wt%. The hypereutectic structure of alloy B has a carbon content of about 3.8 wt%. For alloy C, the hypereutectic structure, the carbon content is about 5.9 wt%. The X-ray diffraction results reported in this work [2] show that Cr-Fe solid solution (α) with a body centered cubic structure and $(\text{Cr, Fe})_{23}\text{C}_6$ carbide with a complex face centered cubic structure, exist in alloys A and B. Alloy C includes three phases, which are α phase, $(\text{Cr, Fe})_{23}\text{C}_6$ and $(\text{Cr, Fe})_7\text{C}_3$ carbides.

Fig. 2 shows the microstructure characteristics of Cr-Fe-C alloys for different carbon contents. In Fig. 2(a), when the carbon content is present as 2.3 wt%, the primary dendritic Cr-Fe phases (α) form in the surrounding eutectic colonies [$\alpha + (\text{Cr, Fe})_{23}\text{C}_6$]. The microstructure obtained for alloy B, shown in Fig. 2(b), is composed of primary polygonal $(\text{Cr, Fe})_{23}\text{C}_6$ carbides and [$\alpha + (\text{Cr, Fe})_{23}\text{C}_6$] eutectic colonies. Microstructural observations also show that alloy C consists of primary polygonal $(\text{Cr, Fe})_7\text{C}_3$ carbides with hexagonal form and [$\alpha + (\text{Cr, Fe})_7\text{C}_3$] eutectic colonies in Fig. 2(c). Chemical compositions of the individual phases presented in Fig. 2 are analyzed by wavelength dispersive spectrum (Table 4). This quantitative elemental analysis confirms that the primary phases in hard-facing alloys A-C are Cr-Fe solid solution (α), $(\text{Cr, Fe})_{23}\text{C}_6$ and $(\text{Cr, Fe})_7\text{C}_3$ carbides, respectively. The atomic formula of primary α -phase in alloy A is $\text{Cr}_{3.2}\text{Fe}$. The atomic formulas of primary carbides in alloys B and C are $\text{Cr}_{19.6}\text{Fe}_{3.9}\text{C}_6$ and $\text{Cr}_{6.4}\text{Fe}_{0.7}\text{C}_3$, respectively.

Fig. 3 reveals transmission electron microscopy bright field images and corresponding electron diffraction patterns of the marked areas in Cr-Fe-C alloy with 2.3 wt% carbon content. Two selected area electron diffraction patterns shown in Fig. 3

Table 3 – Chemical compositions of the as-clad Cr-Fe-C alloys.

| Hard-facing alloys | Composition (wt.%) | | | | | | |
|--------------------|--------------------|--------|-------|-------|-------|-------|------|
| | C | Fe | Mn | Si | P | S | Cr |
| A | 2.334 | 18.420 | 0.289 | 0.167 | 0.006 | 0.003 | bal. |
| B | 3.838 | 24.529 | 0.424 | 0.188 | 0.004 | 0.004 | bal. |
| C | 5.905 | 21.125 | 0.338 | 0.129 | 0.008 | 0.003 | bal. |

**Fig. 2 – Scanning electron microscopy micrographs of the Cr-Fe-C alloys with different carbon contents: (a) 2.3 wt%, (b) 3.8 wt% and (c) 5.9 wt%.**

(b) and (d) reveal that α phase with $[1\bar{1}3]$ zone axis and M_{23}C_6 carbide with $[1\bar{1}0]$ zone axis exist in the microstructure. However, a selected area electron diffraction pattern revealed in Fig. 4 (b) displays three rings with d-spacings of 2.17, 1.52 and 1.25 Å, when the carbon content increases to 3.8 wt%. After carefully measuring the d-spacing and inter-planar angle from the pattern, the selected area electron diffraction pattern shown in Fig. 4(d) is indexed to be M_{23}C_6 carbide with the $[253]$ zone axis. Fig. 5 shows typical transmission electron microscopy images and corresponding selected area electron diffraction patterns of the constituent phases in Cr-Fe-C alloys with 5.9 wt% carbon content. A selected area electron diffraction pattern collected from the eutectic α phase displays three rings with d-spacings of 2.17, 1.53, and 1.25 Å (Fig. 5(b)). The corresponding selected area electron diffraction in Fig. 5(d) indicates that the

Table 4 – Chemical compositions of each phase in microstructure.

| Position | Phase | Chemical composition (wt%) | | | | |
|----------|--|----------------------------|-------|------|------|-------|
| | | C | Fe | Si | Mn | Cr |
| 1 | $\alpha(\text{Cr}_{3.2}\text{Fe})$ | 0.42 | 24.66 | 0.10 | 0.31 | 74.51 |
| 2 | $\alpha + \text{M}_{23}\text{C}_6$ | 4.19 | 15.43 | 0.05 | 0.35 | 79.98 |
| 3 | $\text{M}_{23}\text{C}_6(\text{Cr}_{19.6}\text{Fe}_{3.9}\text{C}_6)$ | 5.53 | 16.20 | 0.03 | 0.44 | 77.80 |
| 4 | $\alpha + \text{M}_{23}\text{C}_6$ | 3.91 | 27.30 | 0.15 | 0.54 | 68.10 |
| 5 | $\text{M}_7\text{C}_3(\text{Cr}_{6.4}\text{Fe}_{0.7}\text{C}_3)$ | 8.91 | 8.85 | 0.06 | 0.28 | 81.90 |
| 6 | $\alpha + \text{M}_7\text{C}_3$ | 6.09 | 23.80 | 0.33 | 0.52 | 70.30 |

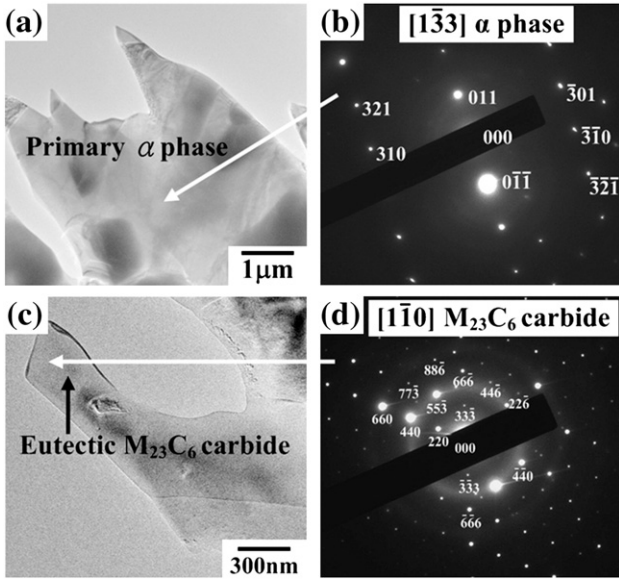


Fig. 3 – Transmission electron microscopy bright field images and corresponding electron diffraction patterns of the marked areas in Cr-Fe-C alloy with 2.3 wt% carbon content.

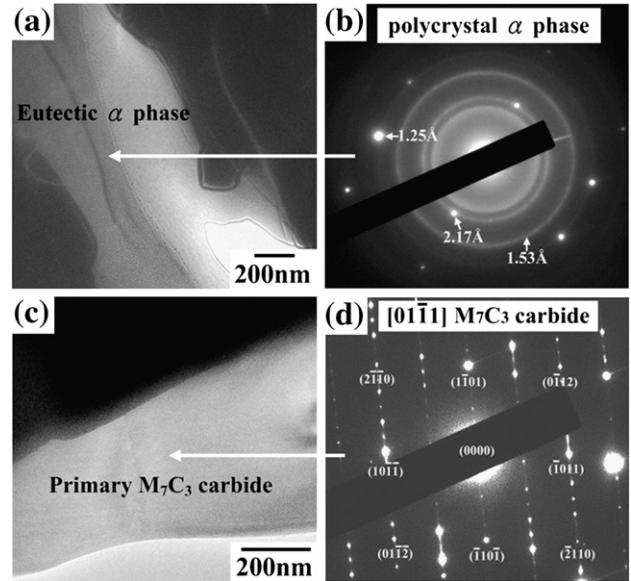


Fig. 5 – Transmission electron microscopy bright field images and corresponding electron diffraction patterns of the marked areas in Cr-Fe-C alloy with 5.9 wt% carbon content.

constituent phase presented in Fig. 5(c) has the M_7C_3 carbide structure with the $[01\bar{1}1]$ zone axis. Summarizing the results of transmission electron microscopy and wavelength dispersive spectrum, microstructures of the as-clad Cr-Fe-C alloys with three different carbon contents consist of α phase, $(Cr,Fe)_{23}C_6$ and $(Cr,Fe)_7C_3$ carbides.

3.2. Morphological Characteristics of the Primary Phases

Fig. 6 reveals the morphological characteristics of various primary phases in Cr-Fe-C alloys. In Fig. 6(a), the morphology of

primary α -phase in alloy A is a non-faceted dendritic structure. The morphologies of primary $(Cr,Fe)_{23}C_6$ and $(Cr,Fe)_7C_3$ carbides in alloys B and C are faceted structures with

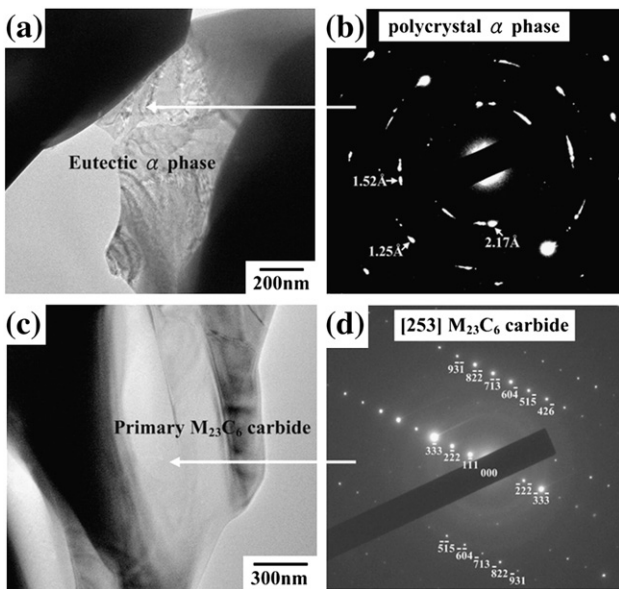


Fig. 4 – Transmission electron microscopy bright field images and corresponding electron diffraction patterns of the marked areas in Cr-Fe-C alloy with 3.8 wt% carbon content.

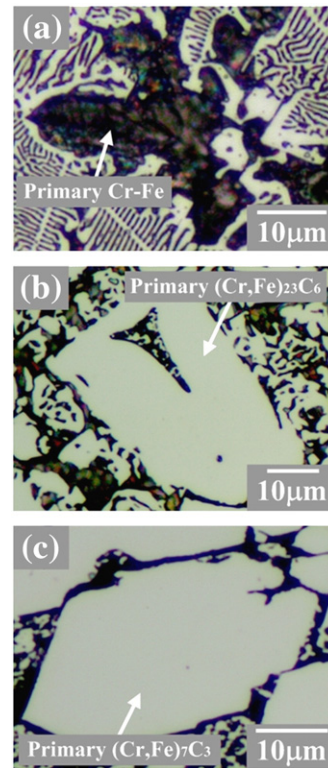


Fig. 6 – Morphological characteristics of the various primary phases in Cr-Fe-C alloys with different carbon contents: (a) 2.3 wt% (primary α -phase), (b) 3.8 wt% (primary $M_{23}C_6$) and (c) 5.9 wt% (primary M_7C_3).

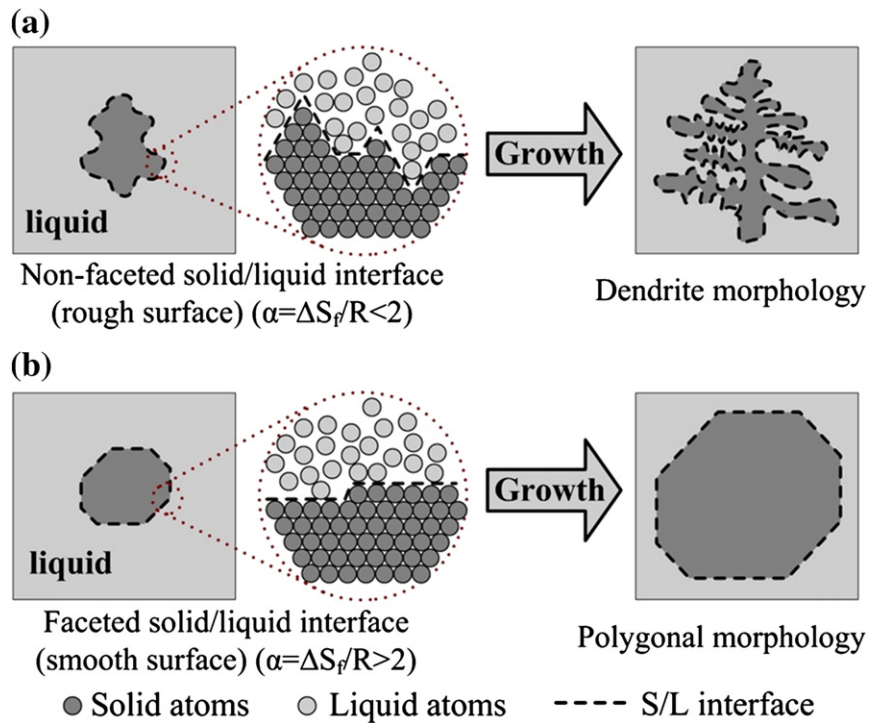


Fig. 7 – The interfacial form between liquid and solid: (a) non-faceted growth and (b) faceted growth.

polygonal shapes, different from the primary α -phase with dendritic shape in alloy A (Fig. 6(b) and (c)). The morphological transition from a primary phase directly depends upon the solid/liquid interfacial form and melting entropy [21]. The various solid/liquid interfacial forms are illustrated in Fig. 7[21]. When the solid/liquid interface at atomic scale is a relatively rough surface, the solid phase assumes a dendritic morphology. By contrast, when the solid/liquid interface at atomic scale is a relatively smooth surface, the solid phase adopts a polygonal morphology.

Fig. 7 also shows the relation between value of α ($=\Delta S_f/R$) and morphological characteristics of the primary phase. Values of α , which are less than two, tend toward non-faceted crystal growth, while higher α -values favor production of faceted growth forms [21]. The α -value of primary α -phase in alloy A is 0.52, predicting a non-faceted solid/liquid interface, as Table 5 shows. Consequently, the primary α -

phase grows with dendritic geometry and has a non-faceted structure. By contrast, the α -values of primary $(\text{Cr,Fe})_{23}\text{C}_6$ and $(\text{Cr,Fe})_7\text{C}_3$ carbides revealed in Table 5 are 15.7 and 3.1, predicting a faceted solid/liquid interface. Therefore, primary $(\text{Cr,Fe})_{23}\text{C}_6$ and $(\text{Cr,Fe})_7\text{C}_3$ carbides adopt into the polygonal shape with faceted structures.

3.3. Electron Backscatter Diffraction Analysis

Fig. 8 presents the obtained electron backscatter diffraction mappings on a hypoeutectic alloy with 2.3 wt% carbon content. The image quality map shown in Fig. 8(a) resembles a backscatter electron image of the sample. The detected image quality values range between 10 and 80. The corresponding phase map presented in Fig. 8(b) shows that the α -phases of primary and eutectic are depicted in red and the eutectic $(\text{Cr,Fe})_{23}\text{C}_6$ carbides in green. The inverse pole figure

Table 5 – Summary of heating and cooling reaction temperatures in the differential scanning calorimeter curves in Fig. 14.

| Alloy | Phases | Heating process | | | Cooling process | | | α |
|-------|--|-----------------|---------------|--------------------|-----------------|---------------|--------------------|----------|
| | | T_{m1} (°C) | T_{m2} (°C) | ΔH_m (J/g) | T_{c1} (°C) | T_{c2} (°C) | ΔH_c (J/g) | |
| A | Cr-Fe | 1478.3 | 1488.5 | -34.1 | 1394.8 | 1391.8 | 17.1 | 0.52 |
| | $\alpha + (\text{Cr,Fe})_{23}\text{C}_6$ | 1380.0 | 1394.6 | -33.3 | 1294.0 | 1291.9 | 2.6 | - |
| B | $(\text{Cr,Fe})_{23}\text{C}_6$ | 1474.6 | 1481.6 | -174.7 | 1366.7 | 1361.3 | 54.7 | 15.7 |
| | $\alpha + (\text{Cr,Fe})_{23}\text{C}_6$ | 1360.8 | 1420.9 | -92.2 | 1218.4 | 1213.8 | 9.3 | - |
| C | $(\text{Cr,Fe})_7\text{C}_3$ | 1416.2 | 1433.5 | -108.3 | 1377.7 | 1370.2 | 143.0 | 3.1 |
| | $\alpha + (\text{Cr,Fe})_7\text{C}_3$ | 1312.5 | 1344.4 | -19.8 | 1223.5 | 1219.6 | 12.3 | - |

T_{m1} , the heating process onset temperature; T_{m2} , the heating process peak temperature; ΔH_m , the melting enthalpy; T_{c1} , the cooling process onset temperature; T_{c2} , the cooling process peak temperature; ΔH_c , the crystallization enthalpy; $\alpha = \Delta S_f/R = \Delta H_m/T_{m1}$; ΔS_f , the entropy of fusion; R, the gas constant.

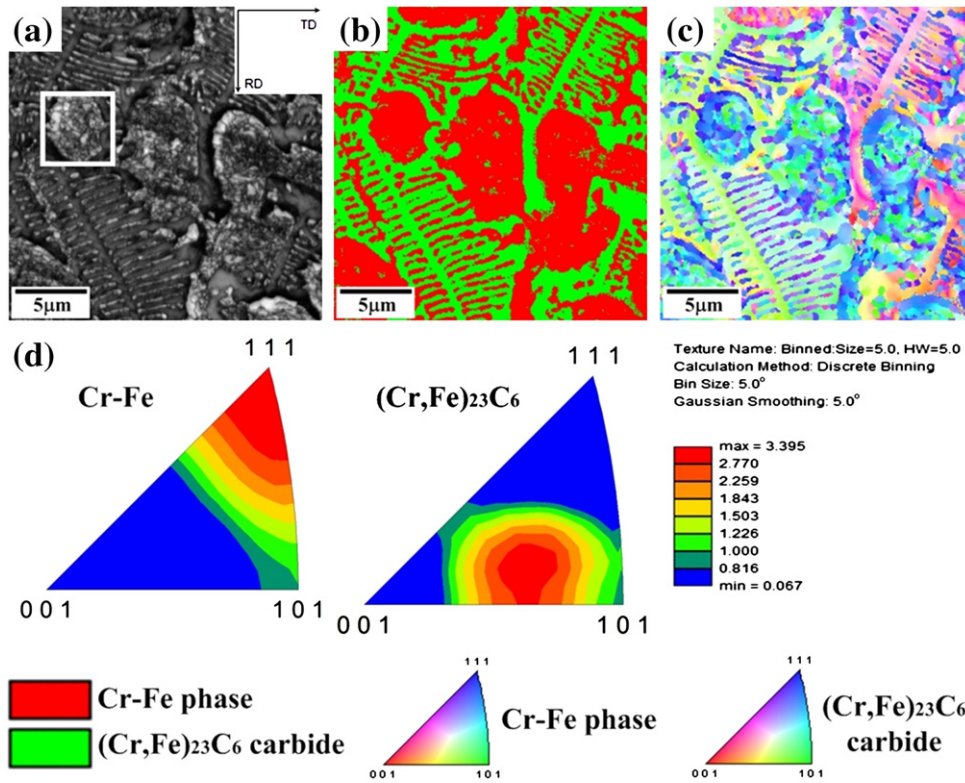


Fig. 8 – (a) Image quality map, (b) phase map, (c) inverse pole figure orientation map in [001] direction (perpendicular to the sample surface) of a hypoeutectic alloy with 2.3 wt% carbon content and (d) gives the inverse pole figures for each phase in [001] direction. In the image quality map, the rolling direction (RD) and transverse direction (TD) are indicated by arrows. The crystallographic orientations of the inverse pole figure map are given by the stereographic triangles.

orientation map in [001] direction is revealed in Fig. 8(c). The α -phases of primary and eutectic exhibit a preferred $\langle 111 \rangle$ crystal direction orientation, as shown in Fig. 8(d). Fig. 9 shows the determined misorientation angle and the grain boundary misorientation angle map of primary α -phase marked in Fig. 8(a). As the misorientation angle ranges from 3° to 20°, the number fraction gradually decays from 0.25 to 0.04, as shown in Fig. 9(a). Nevertheless, the number fraction

reveals the plateau-like behavior, as the misorientation angle is up to 20°. In Fig. 9(b), the high-angle boundaries are decorated with red and black lines (for misorientations > 10°) and can be seen to comprise the majority of the boundaries in primary α -phase grains. The low angle boundaries decorated with orange and deep green (orange lines; less than 5° misorientation) exist in the sub-grain. On the basis of above data, the primary α -phase with relative random orientation

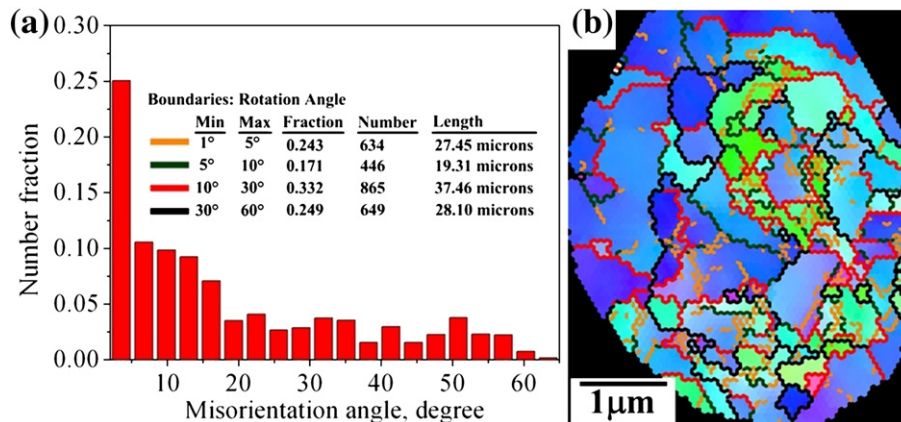


Fig. 9 – Characteristics of the grain boundary misorientation angle for primary α -phase marked in Fig. 8(a): (a) the number fractions of different misorientation angle and (b) the grain boundary misorientation angle map.

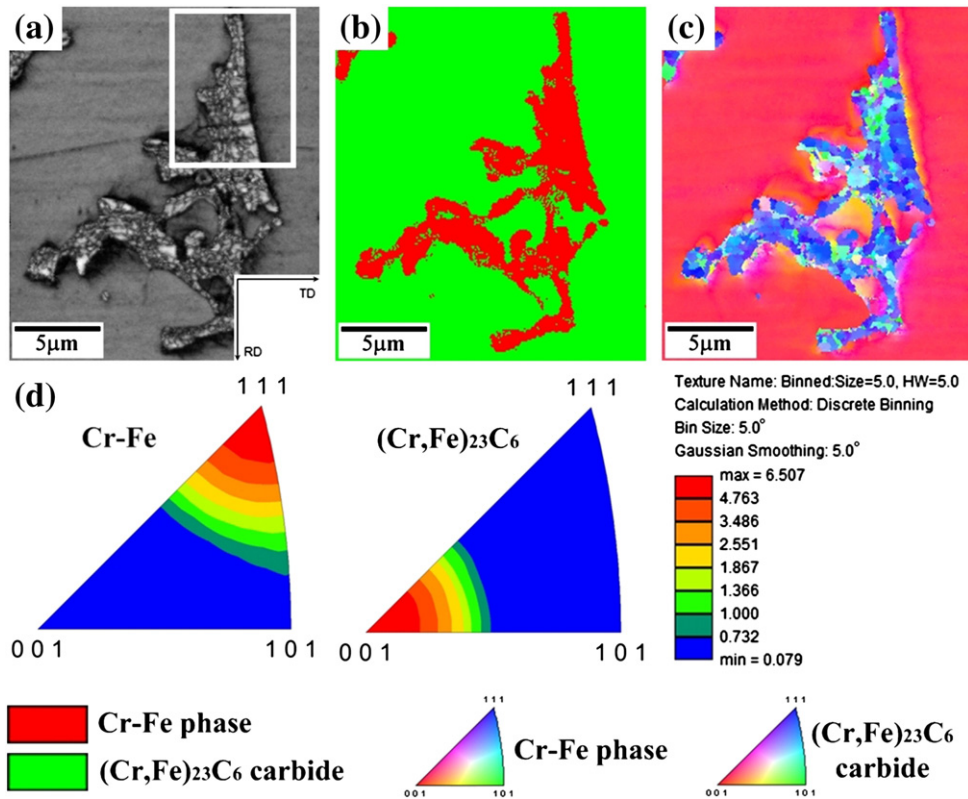


Fig. 10 – (a) Image quality map, (b) phase map, (c) inverse pole figure orientation map of a hypoeutectic alloy with 3.8 wt% carbon content and (d) gives the inverse pole figures for each phase. The crystallographic orientations of the inverse pole figure map are given by the stereographic triangles.

exhibits a polycrystalline structure and comprises a massive high-angle boundary, caused by the dendritic growth mechanism.

Fig. 10 shows the obtained electron backscatter diffraction mappings on a hypereutectic alloy with 3.8 wt% carbon content. The detected image quality values, presented in Fig. 10 (a), range between 60 and 470. The corresponding phase map is indicated in Fig. 10(b). The eutectic α -phase is described in red and the $(Cr,Fe)_{23}C_6$ carbides of primary and eutectic in

green. The inverse pole figure orientation map in [001] direction illustrates in Fig. 10(c). The primary $(Cr,Fe)_{23}C_6$ carbide has a preferred $\langle 001 \rangle$ crystal direction orientation and the eutectic α -phase appears a preferred $\langle 111 \rangle$ crystal direction orientation, as revealed in Fig. 10(d). The determined misorientation angle for primary $M_{23}C_6$ carbide illustrates in Fig. 11(a). It can be seen that the majority of misorientation angle is given in the range of 1-10°, while only a small number of high-angle grain boundaries is observed. The grain

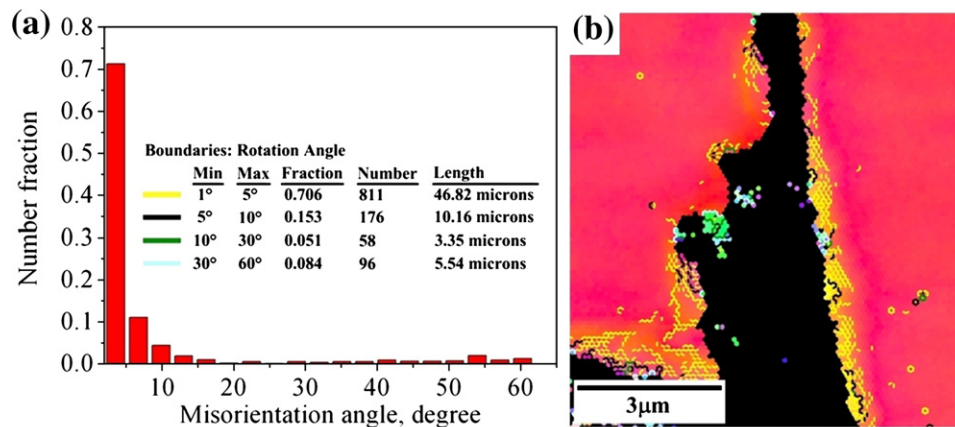


Fig. 11 – Characteristics of the grain boundary misorientation angle for primary $(Cr,Fe)_{23}C_6$ carbide marked in Fig. 10(a): (a) the number fractions of different misorientation angle and (b) the grain boundary misorientation angle map.

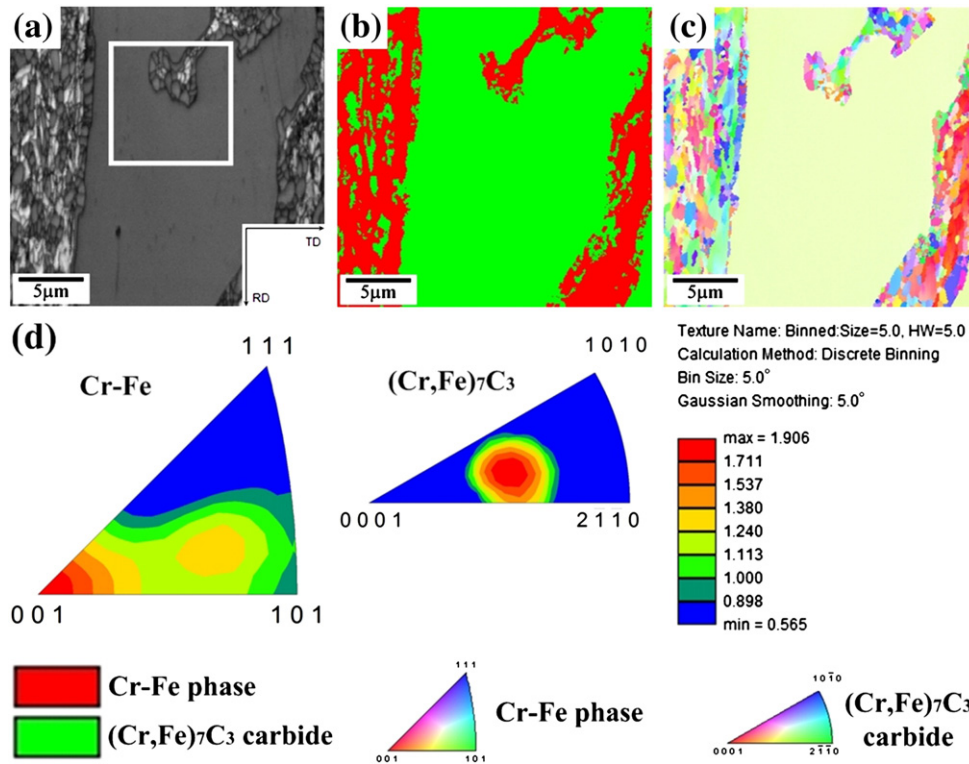


Fig. 12 – (a) Image quality map, (b) phase map, (c) inverse pole figure orientation map of a hypoeutectic alloy with 5.9 wt% carbon content and (d) gives the inverse pole figures for each phase. The crystallographic orientations of the inverse pole figure map are given by the stereographic triangles.

boundary misorientation angle map reveals important details of primary (Cr,Fe)₂₃C₆ carbide, as shown in Fig. 11(b). The low angle boundaries are decorated with yellow and black lines (yellow lines; less than 5° misorientation) and can be seen to consist of the majority of the boundaries in primary (Cr, Fe)₂₃C₆ carbide grain. However, great amounts of low angle boundaries occur between primary (Cr,Fe)₂₃C₆ carbide and eutectic [α+(Cr,Fe)₂₃C₆]. The primary (Cr,Fe)₂₃C₆ carbide with strong texture exists a single crystal structure and contains a

slight low angle boundary, resulting in the polygonal growth mechanism.

Fig. 12 shows the obtained electron backscatter diffraction mappings on a hypereutectic alloy with 5.9 wt% carbon content. The detected image quality values, presented in Fig. 12 (a), range between 10 and 100. The corresponding phase map indicated in Fig. 12(b) illustrates that the eutectic α-phase is described in red and the (Cr,Fe)₇C₃ carbides of primary and eutectic in green. The inverse pole figure orientation map in

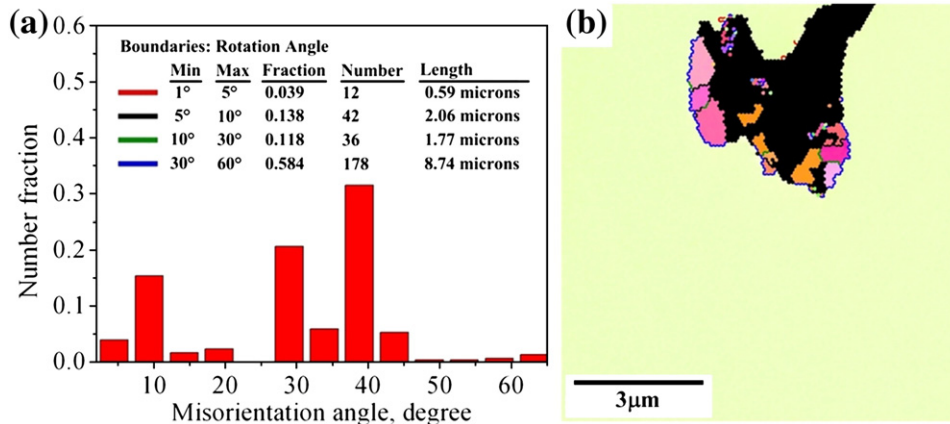


Fig. 13 – Characteristics of the grain boundary misorientation angle for primary (Cr,Fe)₇C₃ carbide marked in Fig. 12(a): (a) the number fractions of different misorientation angle and (b) the grain boundary misorientation angle map.

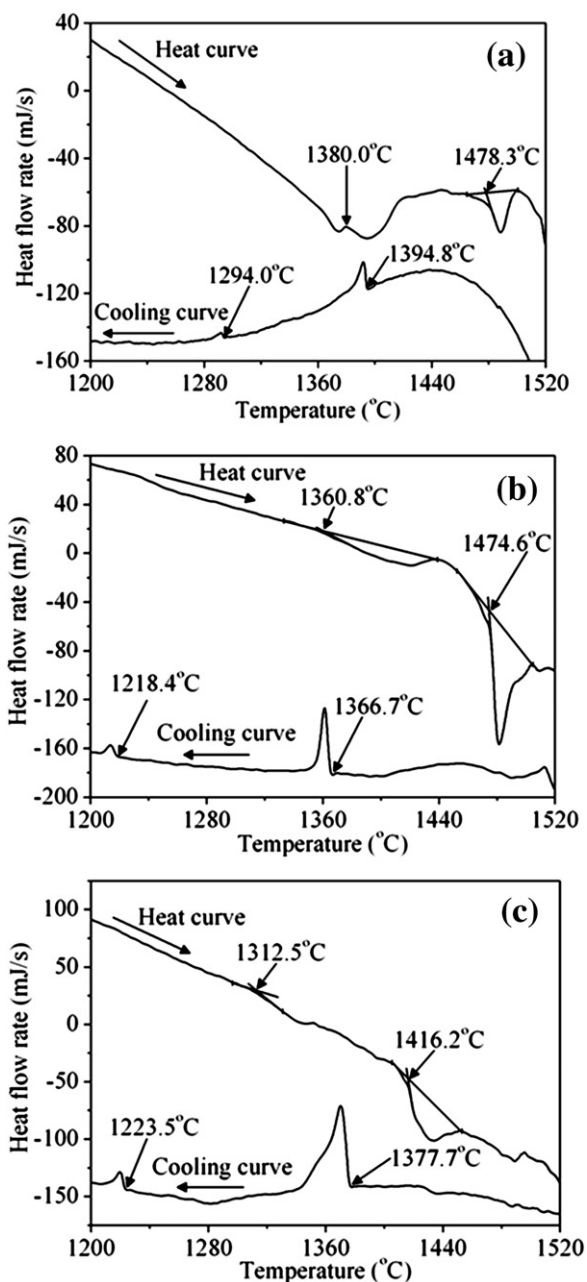


Fig. 14 – Differential scanning calorimeter curves of the Cr-Fe-C alloys with different carbon contents: (a) 2.3 wt%, (b) 3.8 wt% and (c) 5.9 wt%.

[001] direction shows that the eutectic α -phase exhibit a relative random orientation and the primary $(\text{Cr,Fe})_7\text{C}_3$ grain exists a strong texture (Fig. 12(c)). The eutectic α -phase, revealed in Fig. 12(d), exhibits a relatively preferred $\langle 001 \rangle$ crystal direction orientation. In Fig. 13(a), the misorientation angle of primary $(\text{Cr,Fe})_7\text{C}_3$ carbide exhibits a maximum at 39° , followed by some smaller maximum at 29° and 9° . The grain boundary misorientation angle map for primary $(\text{Cr, Fe})_7\text{C}_3$ carbide, shown in Fig. 13(b), indicates that the primary $(\text{Cr,Fe})_7\text{C}_3$ grain has no any boundaries. The high angle boundaries, decorated with blue and green lines, occur among primary, eutectic and eutectic $(\text{Cr,Fe})_7\text{C}_3$ carbides. The primary $(\text{Cr,Fe})_7\text{C}_3$ carbide with strong texture exists a

single crystal structure and has no any boundaries, leading to the polygonal growth mechanism.

3.4. Solidification Behavior

Fig. 14 shows the differential scanning calorimeter curves for Cr-Fe-C alloys with three different carbon compositions. Table 5 summarizes the differential scanning calorimeter results shown in Fig. 14 during heating and cooling process. Fig. 14(a) reveals that Cr-Fe-C alloy with 2.3 wt% carbon content has two exothermic peaks in cooling curve. The onset temperature of first peak at 1394.8°C is due to the formation and growth of primary α -phase. At lower temperature, the second exothermic peak is seen at 1294.0°C , caused by the formation of eutectic $[\alpha + (\text{Cr,Fe})_{23}\text{C}_6]$. Differential scanning calorimeter obtained for Cr-Fe-C alloy with 3.8 wt% carbon content reveals the first exothermic peak at 1366.7°C , when the formation and growth of primary $(\text{Cr,Fe})_{23}\text{C}_6$ carbide occurs (Fig. 14(b)). With continuous decrease in temperature, a second exothermic peak is seen at 1218.4°C , which is attributed to the formation of eutectic $[\alpha + (\text{Cr,Fe})_{23}\text{C}_6]$. When the carbon content reaches to 5.9 wt%, the cooling curve shows the initial phase transition temperature at 1377.7°C , corresponding to the formation and growth of primary $(\text{Cr,Fe})_7\text{C}_3$ carbide, as Fig. 14(c) presents. A second phase transition temperature at 1223.5°C ensues from the formation of eutectic $[\alpha + (\text{Cr,Fe})_7\text{C}_3]$.

4. Conclusion

Electron backscatter diffraction technique has been applied successfully to analyze crystallographic orientation and grain boundary misorientation of the constituent phases in Cr-Fe-C alloys with three different carbon concentrations. The morphology of primary phase transits from dendritic shape with non-faceted structure to polygonal shape with faceted structure, as the carbon content varies from 2.3 to 5.9 wt%. The primary $(\text{Cr,Fe})_{23}\text{C}_6$ and $(\text{Cr,Fe})_7\text{C}_3$ carbides with strong texture exist a single crystal structure and contain a slight low angle boundary, resulting in the polygonal growth mechanism. Nevertheless, the primary α -phase with relative random orientation exhibits a polycrystalline structure and comprises a massive high-angle boundary, caused by the dendritic growth mechanism. Phase transitions during solidification process also have been investigated by differential scanning calorimeter. In Cr-18.4Fe-2.3 C alloy, the primary α -phase solidifies at 1394.8°C and eutectic colony forms at 1294.0°C . When the carbon content increases to 3.8 wt%, the structure contains primary $(\text{Cr,Fe})_{23}\text{C}_6$ carbide solidified at 1366.7°C and eutectic $[\alpha + (\text{Cr,Fe})_{23}\text{C}_6]$ formed at 1218.4°C . When the carbon content reaches to 5.9 wt%, primary $(\text{Cr,Fe})_7\text{C}_3$ carbide and eutectic $[\alpha + (\text{Cr,Fe})_7\text{C}_3]$ form at 1377.7°C and 1223.5°C , respectively.

Acknowledgements

The authors would like to thank the financial support of Ministry of Economic Affairs and National Science Council under projects numbered 99-EC-17-A-08-S1-117 and NSC99-2221-E-005-033-MY3.

REFERENCES

- [1] Lin CM, Chang CM, Chen JH, Wu W. The effects of additive elements on the microstructure characteristics and mechanical properties of Cr-Fe-C hard-facing alloys. *J Alloys Compd* 2010;498:30–6.
- [2] Lin CM, Chang CM, Chen JH, Hsieh CC, Wu W. Microstructural evolution of hypoeutectic, near-eutectic, and hypereutectic high-carbon Cr-based hard-facing alloys. *Metall Mater Trans A* 2009;40:1031–8.
- [3] Fan C, Chen MC, Chang CM, Wu W. Microstructure change caused by (Cr,Fe)₂₃C₆ carbides in high chromium Fe–Cr–C hardfacing alloys. *Surf Coat Technol* 2006;201:908–12.
- [4] Kuo CW, Fan C, Wu SH, Wu W. Microstructure and wear characteristics of hypoeutectic, eutectic and hypereutectic (Cr,Fe)₂₃C₆ carbides in hardfacing alloys. *Mater Trans* 2007;48:2324–8.
- [5] Yilmaz SO. Wear behavior of gas tungsten arc deposited FeCr, FeCrC, and WC coatings on AISI 1018 steel. *Surf Coat Technol* 2006;201:1568–75.
- [6] Yilmaz SO. Wear behavior of gas tungsten arc deposited FeCrC, FeCrSi, and WCo coatings on AISI 1018 steel. *Surf Coat Technol* 2005;194:175–83.
- [7] Lu B, Luo J, Chiovelli S. Corrosion and wear resistance of chrome white irons-A correlation to their composition and microstructure. *Metall Mater Trans A* 2006;37:3029–38.
- [8] Lin CM, Chang CM, Chen JH, Hsieh CC, Wu W. Microstructure and wear characteristics of high-carbon Cr-based alloy claddings formed by gas tungsten arc welding (GTAW). *Surf Coat Technol* 2010;205:2590–6.
- [9] Luan Y, Song N, Bai Y, Kang X, Li D. Effect of solidification rate on the morphology and distribution of eutectic carbides in centrifugal casting high-speed steel rolls. *J Mater Process Technol* 2010;210:536–41.
- [10] Chang CM, Lin CM, Hsieh CC, Chen JH, Wu W. Micro-structural characteristics of Fe-40wt%Cr-xC hardfacing alloys with [1.0–4.0 wt%] carbon content. *J Alloys Compd* 2009;487:83–9.
- [11] Chen SH, Chen CC, Chao CG. Novel morphology and solidification behavior of eutectic bismuth-tin (Bi-Sn) nanowires. *J Alloys Compd* 2009;481:270–3.
- [12] Fras E, Kawalec M, Lopez HF. Solidification microstructures and mechanical properties of high-vanadium Fe-C-V and Fe-C-V-Si alloys. *Mater Sci Eng A* 2009;524:193–203.
- [13] Xu CL, Wang HY, Liu C, Jiang QC. Growth of octahedral primary silicon in cast hypereutectic Al-Si alloys. *J Cryst Growth* 2006;291:540–7.
- [14] Souza SA, Rios CT, Coelho AA, Ferrandini PL, Gama S, Caram R. Growth and morphological characterization of Al-Cr-Nb eutectic alloys. *J Alloys Compd* 2005;402:156–61.
- [15] Xie H, Jia L, Lu Z. Microstructure and solidification behavior of Cu-Ni-Si alloys. *Mater Charact* 2009;60:114–8.
- [16] Banda W, Georgalli GA, Lang C, Eksteen JJ. Determination of the phase transformation temperatures of the Fe-Co-Cu-Si system in the Fe-rich corner by thermal analysis. *Metall Mater Trans B* 2008;39:655–61.
- [17] Matsubara Y, Sasaguri N, Shimizu K, Yu SK. Solidification and abrasion wear of white cast irons alloyed with 20% carbide forming elements. *Wear* 2001;250:502–10.
- [18] Sreeja Kumari SS, Pillai RM, Rajan TPD, Pai BC. Effects of individual and combined additions of Be, Mn, Ca and Sr on the solidification behaviour, structure and mechanical properties of Al-7Si-0.3Mg-0.8Fe alloy. *Mater Sci Eng A* 2007;460–461:561–73.
- [19] Meng G, Lin X, Huang W. The relationship between effective entropy change and volume fraction of the eutectic phases in eutectic microstructures. *Mater Lett* 2008;62:984–7.
- [20] Taylor MR, Fidler RS, Smith RW. Broken lamellar eutectic growth; Structure of the silver-bismuth eutectic. *J Cryst Growth* 1968;3–4:666–73.
- [21] Kurz W, Fisher DJ. Fundamentals of solidification. Switzerland: Trans Tech Publications; 1984.
- [22] Woodcock TG, Gutfleisch O. Multi-phase EBSD mapping and local texture analysis in NdFeB sintered magnets. *Acta Mater* 2011;59:1026–36.
- [23] Staiger MP, Kolbeinsson I, Newman J, Woodfield T, Sato T. Orientation imaging microscopy of polycrystalline sodium chloride. *Mater Charact* 2010;61:413–9.
- [24] Chen CL, Tatlock GJ, Jones AR. Microstructural evolution in friction stir welding of nanostructured ODS alloys. *J Alloys Compd* 2010;504S:S460–6.
- [25] Lui GT, Chen D, Kuo JC. EBSD Characterization of Twinned Copper Using Pulsed Electrodeposition. *J Phys D: Appl Phys* 2009;42:215410–7.
- [26] Koblischka-Veneva A, Koblischka MR, Qu T, Han Z, Mucklich F. Texture analysis of monofilamentary, Ag-sheathed (Pb,Bi)₂Sr₂Ca₂Cu₃O_x tapes by electron backscatter diffraction (EBSD). *Physica C* 2008;468:174–82.
- [27] Zaefferer S, Kuo JC, Zhao Z, Winning M, Raabe D. On the influence of the grain boundary misorientation on the plastic deformation of aluminum bicrystals. *Acta Mater* 2003;51:4719–35.